https://doi.org/10.5194/egusphere-2024-1099
Preprint. Discussion started: 16 May 2024

Monitoring Summertime Erosion Patterns Over an Arctic Permafrost Coast with Recent Sub-meter Resolution Microsatellite SAR Data

Ya-Lun S. Tsai[1,2]

[1]Earth Observation and Remote Sensing Lab, Surveying and Geospatial Engineering Division, Department of Civil Engineering, National Taiwan University, Taipei 10617, Taiwan
[2]Hydrotech Research Institute, National Taiwan University, Taipei 10617, Taiwan

Correspondence to: Ya-Lun S. Tsai (yalunstsai@ntu.edu.tw)

Abstract. Arctic coasts experience some of the highest rates of erosion in the world, particularly due to permafrost degradation resulting from the recent exacerbation of climate change. Therefore, not only have coastal defense and energy facilities been threatened, but maintenance costs for the infrastructure of cold regions have also risen. To monitor the coastal erosion pattern of the circum-Arctic, earlier studies often employ spaceborne or airborne optical multi-spectral images to depict shoreline changes, which are limited by frequent clouds and haze in Arctic regions and, thus, hamper the time-series analysis. Instead, this study aims to explore the synthetic aperture radar (SAR) images, especially the recently developed microsatellite SAR data, which provide unprecedented high-resolution at a sub-meter scale, to measure the summertime spatio-temporal dynamics of an ice-rich permafrost coast along the Beaufort Sea, Alaska. The results reveal a maximum shoreline change envelope (SCE) of 64.89 m during the three-month study period. To examine the differences between the estimations and the observations derived from the conventional Sentinel-1 data, the proposed multi-stage statistical-driven scheme is used. A statistically significant positive relationship between two depicted SCEs with the presence of heteroscedasticity is confirmed. In detail, the agreement between two SCEs increases with the magnitude of the SCE, indicating that the microsatellite SAR can depict more trivial changes in coastline positions. Founded on the results and detailed discussion on the uniqueness and limitations of current SAR sensors, the promising opportunity to utilize the blooming microsatellite SAR datasets for coastal monitoring is highlighted.

1 Introduction

Permafrost, also known as perennially frozen ground, is the subsurface material composed of soil, ice, sediment, or even bedrock with a variable thickness that remains at or below 0 ° C for at least two consecutive years. Due to unique biogeochemical processing and low decomposition rates, permafrost holds a huge amount of carbon stock. Previous studies estimated that around 1300-1700 Pg of organic carbon (OC) is stored in the Arctic permafrost, accounting for almost half of terrestrial carbon storage globally (Streletskiy et al., 2015). However, due to the recent deterioration of climate change, permafrost stability has been sabotaged, especially considering that the Arctic warming speed is twice the global average because of the Arctic amplification effect (Stocker et al., 2013).

https://doi.org/10.5194/egusphere-2024-1099
Preprint. Discussion started: 16 May 2024

Therefore, among global shorelines, Arctic coasts demonstrate the most severe erosion (Jorgenson and Brown, 2005) and, thus, release large amounts of sequestrated OC into the Arctic Ocean. According to Wegner et al. (2015), coastal erosion results in around 4.9-14.0 Tg/year OC flux, i.e., nearly half of the riverine amount. In fact, a study reports that erosion rates on Arctic Alaskan coasts have doubled since the middle of the twentieth century (Frederick et al., 2016). Even worse, as simulated by Guo and Wang (2016), 72% of the permafrost in Alaska will thaw under the representative concentration pathway (RCP)4.5, which could lead to significant impacts on both terrestrial and marine landscapes.

Consequently, to quantify Arctic coastal erosion, which is an imminent threat to coastal environments and infrastructure (Gibbs and Richmond, 2015), many studies utilize spaceborne or airborne multi-spectral images to depict shoreline changes (Bristol et al., 2021; Jones et al., 2018). Nevertheless, since these remote sensing sensors are passive, their data availability is hindered by cloud cover and haze in Arctic regions, which hampers the time-series analysis. Thus, as recent studies indicate, understanding Arctic coasts' spatiotemporal dynamics remains limited (Frederick et al., 2016; Jones et al., 2018). It impedes modeling the thermodynamic mechanism and geomorphic feedback on OC losses and jeopardizes the forecasting and adaptation of climate change on local ecosystems and communities.

Fortunately, spaceborne synthetic aperture radar (SAR) provides an alternative data source. While SAR data are cloud-free and weather-independent, they are rarely employed for Arctic shoreline monitoring until recently (Bartsch et al., 2020; Philipp et al., 2022). Also, most studies utilize SAR images having a relatively coarse spatial resolution of around 20 m that are acquired with either the classic stripmap or advanced ScanSAR mode, which cannot depict the high spatial heterogeneity of Arctic coastal dynamics. In contrast, the rapid growth of microsatellite-based SAR sensors in recent years that have achieved sub-meter resolution with their spotlight mode grant a unprecedented opportunity. Nonetheless, to the best of the author's knowledge, there is no work that makes use of these novel SAR microsatellite constellations to monitor the Arctic coasts.

Thence, the overall objective of this study is to explore the latest very high-resolution microsatellite-based SAR data for depicting the erosional dynamics of Arctic permafrost coasts, exemplified by an Alaskan coast. It hereby utilizes the shoreline extraction method proposed in Tsai (2024). To investigate the reliability and details of the shoreline changes derived from microsatellite SAR, observations estimated with the relatively coarse resolution conventional SAR data are compared via the proposed robust statistical-based scheme. Lastly, the uniqueness and limitations of microsatellite SAR data relative to conventional SAR sensors are also discussed.

2 Study area and materials

2.1 Study area

The Alaskan permafrost coast exhibits the highest erosive rate among the Arctic and the world, especially along the Beaufort Sea coast (Frederick et al., 2016). This is due to the wide distribution of ice-rich permafrost and the lack of barrier islands (Ravens et al., 2012). Due to the deterioration and retreat of the shoreline, many Alaskan coastal villages and infrastructure have been threatened or relocated (Nicolsky et al., 2017). Regarding the oceanic condition, the Beaufort Sea coast features low

https://doi.org/10.5194/egusphere-2024-1099
Preprint. Discussion started: 16 May 2024

wave energy and a centimeter-scale micro-tidal setting (Gibbs and Richmond, 2015); thence, the tidal effect, i.e., the offsets of shoreline positions resulting from the variations of tidal heights (Tsai and Tseng, 2023), is neglectable.

Specifically, this study focuses on a coast segment extending approximately 3.4 km near McLeod Point, located 7 km east of Drew Point (Fig. 1). It is one of the most erosive coasts along the north slope of Alaska (Gibbs and Richmond, 2015). Even worse, a significant acceleration in rates over decades has been reported in recent studies (Jones et al., 2018; Tsai, 2024). The landscape at the site is characterized by ice wedges, thermokarst lakes, and drained thaw lake basins (DTLBs), stemming from the thermo-mechanical erosion of ice-rich permafrost (Frohn et al., 2005). Because of the exacerbated coastal erosion and low-lying bluffs, frequent inundation causes brown-looked salt-killed tundra and overwash of sediments inland (Gibbs and Richmond, 2015). Similar to other Alaskan permafrost coasts, the erosion at this coastal segment takes place mainly in the sea ice-free summertime season owing to the storm and wave-leading thermo-abrasion and the resultant block failure (Jones et al., 2009).

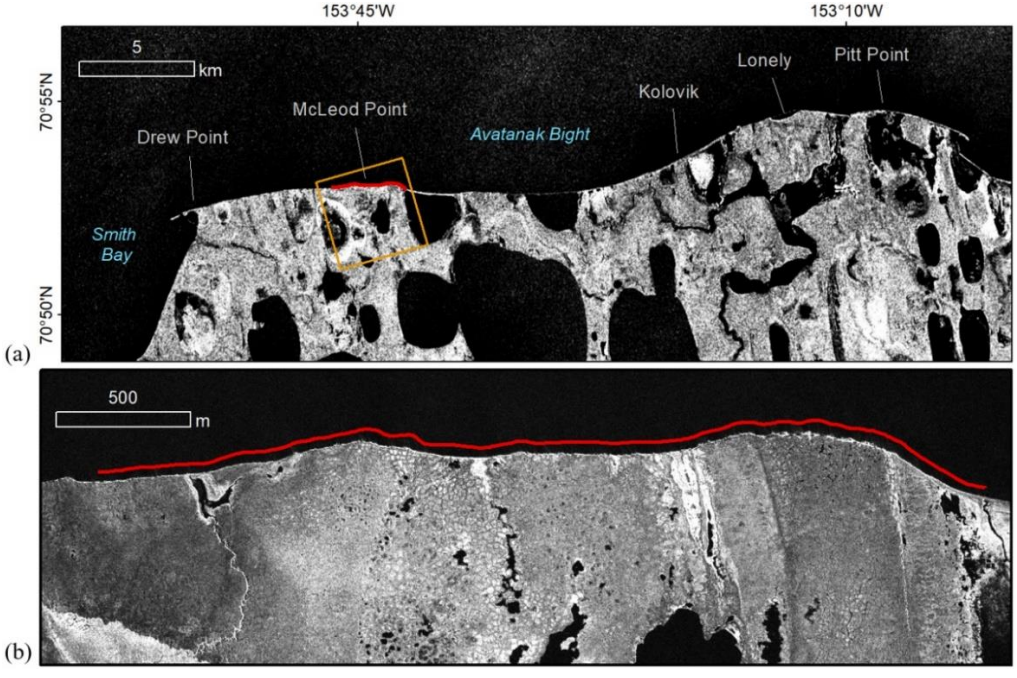

Figure 1: The geographical location of the study coast (red line) near McLeod Point, Alaska. The employed Sentinel-1 and Umbra images are demonstrated in (a) and (b), respectively. The coverage of Umbra SAR images is represented as the orange polygon in (a).

2.2 Spaceborne SAR datasets

2.2.1 Microsatellite-based SAR images

The number of available SAR sensors has been dramatically increasing in recent decades because of national space agencies and the private sector (Morgan et al., 2020). Specifically, in the aspect of hardware, these SAR imagery companies, such as ICEYE, Capella Space, Umbra Lab, Synspective, iQPS, XpressSAR, and PredaSAR, focus on developing near or sub-100 kg

https://doi.org/10.5194/egusphere-2024-1099
Preprint. Discussion started: 16 May 2024

SAR microsatellites constellations that are less expensive. These SAR sensors predominantly operate in the X band because high-frequency signals have many merits: (1) it provides a finer spatial resolution in the azimuth direction, as the beamwidth of a specific aperture length is proportional to the wavelength, (2) it provides a finer spatial resolution in the range direction, as high-frequency spectrum is less congested than the commonly used low-frequency spectrum, and thus allows a wider bandwidth to generate a shorter pulse. As a result, these microsatellite-based SAR sensors provide very high resolution (≤ 1 m) images and, thus, enable more detailed ground surface change detection.

In this study, the Umbra SAR constellation developed by an Earth observation startup, Umbra Lab, is employed. Its first microsatellite is launched in 2021, and currently there are eight satellites with Initial Operational Capability (IOC) on a near-polar orbit with a nominal orbital height of 560 km. More importantly, Umbra SAR sensors make use of an exceptionally wide bandwidth of up to 1,200 MHz. Thus, an ultra-high resolution from 1 m to 0.25 m is achievable in their spotlight acquisition mode. Regarding the polarization, Umbra provides a single polarization among two co-polarizations (HH and VV), which yields a greater contrast between land and ocean and, therefore, facilitates shoreline detection (Angelliaume et al., 2018). To depict the detailed intra-seasonal dynamics of the study coast, the present study exploits seven Umbra images with a nominal resolution of 0.5 m. These images are acquired bi-weekly during the landfast sea ice-free summertime (June to October) when most erosion occurs. The VV polarization is selected to align with the Sentinel-1 images. The metadata of the used Umbra images is summarized in Table 1.

2.2.2 Sentinel-1 images

To examine the results extracted from high-resolution Umbra images, conventional Sentinel-1 data maintained by the European Space Agency (ESA) are used. The Sentinel-1 constellation currently consists of Sentinel-1A and -1B, launched in 2014 and 2016, respectively. However, the operation of the latter has been terminated since December 2021 due to a power anomaly. Compared to the 70 kg-weighted Umbra microsatellite that transmits approximately 500 watts, the 2.3 ton-weighted Sentinel-1 has a peak power of up to 4.3 kW (Anghel et al., 2019). Consequently, Sentinel-1 guarantees a better signal-to-noise ratio (SNR) and a wider swath width. In this study, nine Sentinel-1 images acquired with the interferometric wide (IW) swath mode with a nominal resolution of 20 × 5 m are employed. They are acquired approximately during the same summertime period as the Umbra data, with detailed dates summarized in Table 1.

Table 1. The metadata of the employed SAR datasets.

SAR sensor	**Umbra**	**Sentinel-1**
Platform type	Microsatellite	Large satellite
Wavelength	X-band	C-band
Acquisition mode	Spotlight	Interferometric Wide (IW)
Product type	Geo-ellipsoid Corrected (GEC)	Ground Range Detected (GRD)

https://doi.org/10.5194/egusphere-2024-1099
Preprint. Discussion started: 16 May 2024

Multi-look factor (range × azimuth)	1 × 1	5 × 1
Polarization	VV	VV
Average incidence angle	30.8°	37.7°
Average ground resolution (range × azimuth) (m)	0.65 × 0.65	20.4 × 22.5
Acquisition date	2023/6/25	2023/6/25
	2023/7/26	2023/7/7
	2023/8/9	2023/7/19
	2023/8/21	2023/7/31
	2023/9/6	2023/8/12
	2023/9/20	2023/8/24
	2023/10/4	2023/9/5
		2023/9/17
		2023/9/29

3 Methodology

3.1 SAR image pre-processing and co-registration

Since different SAR sensors have diverse specifications and product types, their pre-processing workflows vary. For Sentinel-1 GRD data, firstly, the state vectors are corrected with the precise orbit files with a three-dimensional root-mean-square (RMS) of less than five centimeters, and then the thermal noises are removed. Next, the stored amplitude is radiometrically calibrated to gamma nought, which shows the least incidence angle- and topography-dependency. Because no precise digital elevation model (DEM) is available (considering the rapid change of landscape), the terrain-flattened normalization is not performed. Lastly, an average ellipsoidal height-based range-Doppler correction is conducted to geocode and orthorectify slant-range SAR images. On the other hand, because Umbra GEC data are already geocoded and ellipsoid-based terrain corrected, no further steps are performed.

Based on both SAR sensors' geocoded amplitude images, the next step is to co-registrate each stack at a sub-pixel accuracy. Practically, it is fulfilled with a two-stage cross-correlation using a large/small window size and a small/large oversampling factor, respectively. This step is straightforward for Sentinel-1 images that have stringent orbital precision and a narrow orbital tube (RMS of less than 100 m in radius) (Geudtner et al., 2016), guaranteeing precise geocoding. In contrast, Umbra satellites have poorer orbital repeatability and result in unsatisfying geocoding accuracy; thus, they must be co-registrated with a reference image with reliable geometrical precision, e.g., Sentinel-1. However, because 20 m-resolution Sentinel-1 images are

https://doi.org/10.5194/egusphere-2024-1099
Preprint. Discussion started: 16 May 2024

much coarser than the 0.5 m-resolution Umbra images, they cannot be used as the reference (although in this study, co-registrated Sentinel-1 images are resampled to the exact resolution of Umbra images to facilitate shoreline mapping at a sub-pixel scale). Therefore, an additional VV-polarized spotlight TerraSAR-X image acquired on 2023/10/6 is used, which has a reliable geometric accuracy and high spatial resolution. To co-registrate the stack of Umbra images, this TerraSAR-X image is first radiometrically calibrated and geocoded. Considering the varying offsets and geometric distortions between Umbra images, a polynomial warping function is used for the co-registration. Eventually, via visual inspections, there is no visible offset among co-registrated Umbra images.

3.2 SAR-based feature extraction and shoreline mapping

Because SAR images suffer from random interference-caused speckle, it is necessary to further enhance the contrast of backscattered intensity between the ocean surface and land. Therefore, the SAR-derived feature extraction and shoreline mapping approach proposed in Tsai (2024) is followed. Firstly, the intensity is logarithmically converted to decibel units, i.e., decibel images, which compress the wide value range and, thus, highlight the overall boundary of ocean/land. Next, the second-order Grey Level Co-occurrence Matrix (GLCM) variance is extracted from the co-occurrence of pixel values with a moving window of 5×5 and a pixel displacement of 1 in all directions. It not only explains approximately 95% of the absolute loadings among all GLCM features to the first principal component analysis (PCA) component exhibiting the most significant contrast between ocean/land but also mitigates the influences of speckle and yields less noisy shorelines (Tsai, 2024). Then, based on the co-registrated GLCM variance, time-series shorelines are mapped with the morphological active contours without edges (MorphACWE) algorithm (Marquez-Neila et al., 2013). This method iteratively evolves an elastic curve to depict the ocean and land boundary, eventually yielding a smooth and continuous shoreline. Consequently, multi-temporal shorelines can be extracted from stacked Umbra and Sentinel-1 images.

Whilst the approach mentioned above can be applied to conventional SAR datasets as demonstrated in Tsai (2024), it is unsuitable for microsatellite SAR images for two reasons: (1) high-resolution SAR images bear severer speckle. This is because compared with the conventional coarse-resolution SAR images, the number of scatterers in each resolution cell is much fewer in high-resolution SAR images; therefore, the speckle pattern does not obey the Goodman statistical model. In consequence, a larger variation of backscattered phase (and the resultant intensity) between pixels over a homogenous surface (e.g., beaches or the ocean surface) is evident and, thus, conventional fully developed speckle-targeted filters (e.g., Lee filter) cannot achieve an ideal performance (Xu et al., 2018). (2) microsatellite SAR images have a higher (i.e., poorer) system-caused background noise, i.e., the noise-equivalent sigma zero (NESZ). It is due to the fact that although most microsatellite SAR operate in relatively low orbital attitudes, they have much lighter weights and thus, inevitably use a shorter antenna and deliver a weaker transmit power (Patyuchenko et al., 2009).

To mitigate the influences of severer speckle and poorer NESZ of microsatellite SAR images, the mapped shorelines are further generalized with the polynomial approximation with exponential kernel (PAEK) algorithm (Bodansky et al., 2002). This method guarantees the smoothing of vectors while maintaining local geometric consistency. Hence, it is commonly used for

https://doi.org/10.5194/egusphere-2024-1099
Preprint. Discussion started: 16 May 2024

post-processing optical image-derived shorelines (Ferrer-Valero, 2018; Sayre et al., 2019). Yet, it is rarely used for SAR-based shoreline mapping studies.

3.3 Coastal erosion assessment and cross-SAR sensor comparison

Founded on the multi-temporal shorelines retrieved from both Umbra and Sentinel-1 images, coastal erosion dynamics can be quantified. This study employs the Digital Shoreline Analysis System (DSAS) developed by the United States Geological Survey (USGS) (Himmelstoss et al., 2018), which provides a standard workflow for depicting shoreline changes recommended by the Federal Emergency Management Agency (FEMA). In detail, by automatically casting equally spaced transects, DSAS can estimate each coastal segment's spatio-temporal variation with different statistical indices, e.g., shoreline change envelope (SCE) (i.e., the greatest distance among all shorelines) and linear regression rate (LRR). In the present study, transects are cast at a three-meter interval and SCE is utilized rather than LRR because (1) the number of analyzed images is fewer than ten (Table 1); therefore, the uncertainties in LRR would be enlarged and (2) the objective of this study is to depict the maximum shoreline retreating distance among the study summertime instead of monitoring the long-term average change rate.

Consequently, two different SCEs derived from Umbra and Sentinel-1 images can be estimated along the study coast, which are expected to show discrepancies in both patterns and magnitudes. Theoretically, the SCE derived from Umbra images is more accurate, as the spatial resolution of Umbra images is more than tenfold higher than the Sentinel-1 images. Therefore, examining the agreement and uniqueness of the two SCEs is necessary. To achieve this goal, this study proposes a statistically reliable and multi-stage scheme to compare these two SCEs, elaborated as follows.

Firstly, statistical metrics are computed, including median absolute deviation (MAD), mean absolute error (MAE), and root-mean-square error (RMSE). These metrics provide quantitative measurements of two SCEs' similarity with different pros and cons, such as sensitivity to outliers. Therefore, the overall difference between the two results can be revealed. Next, assuming that both SCEs share a linear relationship, a linear regression analysis is used to fit the observations. The R-squared value is computed and the overall F-test is conducted to assess the fitness (i.e., explained variances) of the linear regression model. Furthermore, Pearson's correlation analysis is calculated, which also assumes a linear relationship. Yet, to examine the bivariate normal distribution required by Pearson's correlation, Kolmogorov-Smirnov (K-S) and Shapiro-Wilk tests are performed on both SCEs to verify their normality.

However, considering that both SCEs may be non-normal and share a non-linear relationship, non-parametric correlation tests are also performed, i.e., Spearman's and Kendall's rank tests. These tests do not make assumptions about the data distribution and, thus, can handle skewed data and are less sensitive to outliers. Next, apart from the overall correlations, it is critical to investigate whether the correlation between two SCEs varies with the magnitude of Umbra- or Sentinel-1-based SCE. Namely, the fourth step is to examine the homoscedasticity (i.e., the variances of differences between two SCEs), which is fulfilled by performing the Breusch-Pagan and White tests.

In addition to detecting the presence of heteroscedasticity, the trend and magnitude of the heteroscedasticity are explored via segmented correlation analysis and conditional quantile regression. The former requires analyzers to manually split the data

https://doi.org/10.5194/egusphere-2024-1099
Preprint. Discussion started: 16 May 2024

into several subsets based on the value of Umbra-derived SCE and then conduct the correlation analysis with each subset. To avoid uncertainties caused by manual interventions, this study uses quantile values for data segmentation. In contrast, the latter automatically splits the data into several subsets based on the quantiles of the Sentinel-1-derived SCE and then performs regression with each subset. Based on the trend of coefficients revealed in both analyses, the pattern of heteroscedasticity can be revealed. Noteworthily, all statistical tests in these five steps are conducted at a 95% confidence level.

4 Results and discussion

4.1 Summertime erosional SCE estimated with SAR datasets

Fig. 2 illustrates the SCEs of all 1137 transects depicted with Sentinel-1 and high-resolution Umbra images during a three-month summer period (from June to September 2023, as listed in Table 1). A similar maximum SCE retreating distance is estimated from both Sentinel-1 (66.04 m) and Umbra (64.89 m) images. Geographically, these highly erosive transects are sparsely distributed on the western part of the study coast. In contrast, transects exhibiting minimum SCE dominantly lie on the east end of the study coast, with a value of 4.94 (Sentinel-1) and 9.56 m (Umbra), respectively. When it comes to the median values, the two SCEs differ considerably (24.49 and 34.88 m for Senintel-1 and Umbra, respectively). These descriptive statistics agree with the visual interpretation of both SCE patterns. Namely, they are generally comparable, while differences in details are noticeable. This finding is expected, as two SAR datasets have significantly different spatial resolutions. Indeed, more coastal and geomorphological details can be identified with the sub-meter scale Umbra images than with 20 m-resolution Sentinel-1 images, as exemplified by the discernible ice-wedge polygons and widely scattered thermokarst lakes in Fig. 2(a).

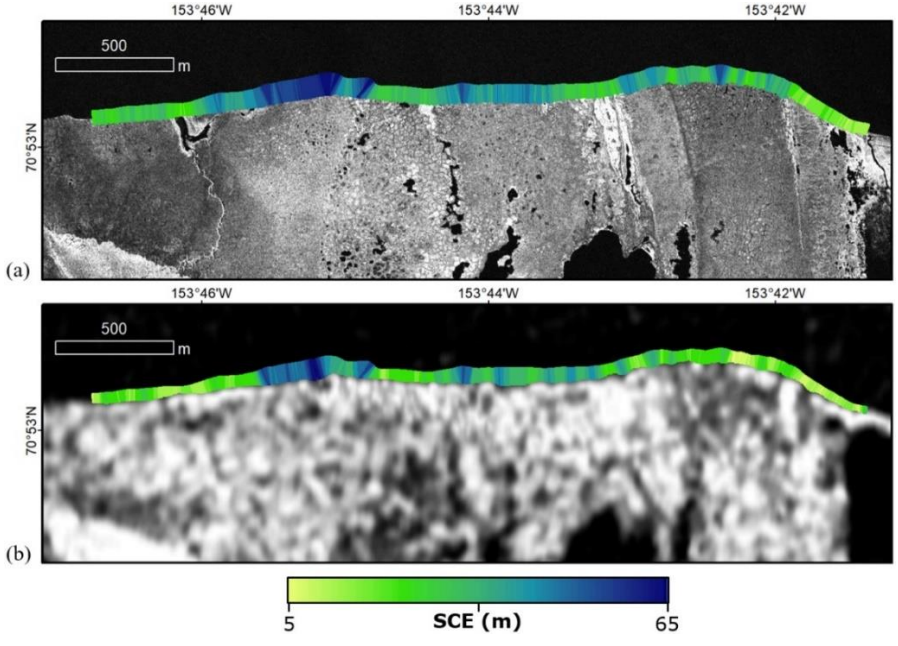

https://doi.org/10.5194/egusphere-2024-1099
Preprint. Discussion started: 16 May 2024

Figure 2: Estimated SCE based on (a) high-resolution Umbra and (b) Sentinel-1 images during June to September 2023

4.2 Statistical-based comparison of cross-SAR sensor-derived SCEs

The proposed statistical-based scheme is applied to examine the differences between two estimated SCEs robustly. In step one, three different statistical metrics are computed. The MAD, MAE, and RMSE are 9.22, 10.36, and 12.50 m, respectively. Firstly, the order of their magnitudes is reasonable, as MAD represents the median of the absolute difference, MAE represents the average absolute difference, and RMSE denotes the square of the difference. Considering the speckle of both SAR images inevitably introduce noises in the extracted SCEs, i.e., outliers, the largest value of square error compared to average and median errors are expected. Secondly, it is observed that the values of these metrics are all less than a pixel of Sentinel-1 images (approximately 20 m), implying (1) the utilized shoreline mapping approach can guarantee a sub-pixel precision and (2) the overall consistency between two extracted SCEs is affirmed.

Next, in step two, a linear regression model is used to fit both SCEs, as plotted in Fig. 3. An R-squared value of 0.55 suggests a moderate agreement between the two estimations. Also, an overall F-test yielding an F-statistic of 1347.57 with a p-value considerably less than 0.001 indicates the linear model is statistically significant, i.e., the Umbra-derived SCE can significantly explain the variations of Sentinel-1-derived SCE. However, by inspecting the regression line shown in Fig. 3 and the intercept of the regression model (-1.62 m), it is identified that the Sentinel-1-derived SCE is overall slightly smaller than the Umbra-based SCE, suggesting the former's potential underestimations.

Apart from the regression model, the linear relationship-assumed Pearson's correlation analysis is also performed. A resultant coefficient of 0.74 and a p-value much smaller than 0.001 reveal a significant strong positive linear relationship between the two SCEs. Noteworthily, since both SCEs do not follow a normal distribution (as both variables' K-S and Shapiro-Wilk tests' p-values are less than 0.05), Pearson's correlation could be underpowered (i.e., poor Type I error rate control), although the large sample size (1137 transects) might alleviate this problem according to the central limit theorem (Bishara and Hittner, 2017, 2012).

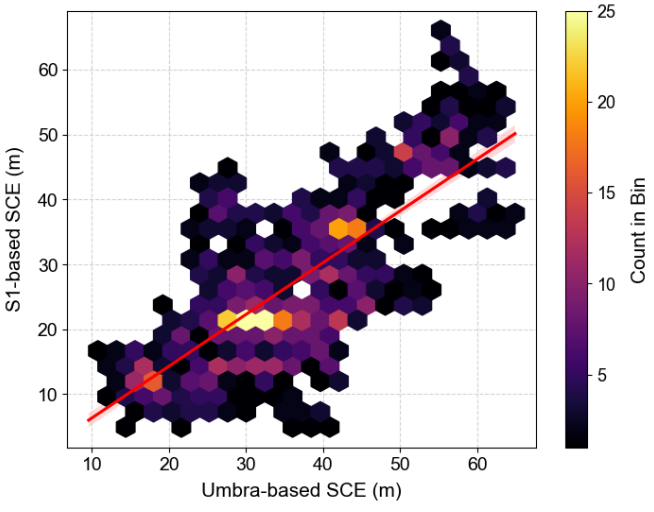

https://doi.org/10.5194/egusphere-2024-1099
Preprint. Discussion started: 16 May 2024

Figure 3: Distribution of the Umbra- and Sentinel-1-derived SCEs and the established linear regression line with the confidence interval at a 95% confidence level.

Therefore, in step three, nonparametric correlation measures, i.e., Spearman's and Kendall's rank tests, which can handle non-normality and non-linearity, are employed. The resultant correlation coefficients of the former and latter are 0.70 and 0.51, respectively, with both p-values significantly smaller than 0.001. Firstly, the relatively lower value of Kendall's Tau than Spearman's is expected, as it is more conservative in estimating the correlation. Secondly, both correlation coefficients affirm the statistical significance of the moderate to strong positive monotonic relationship (i.e., not necessarily linear) between both SCEs. Lastly, since Spearman's rank correlation (0.70) is not considerably greater than Pearson's (0.74), the relationship between two SCEs is presumably not non-linear but generally linear.

Next, in step four, to explore whether the correlation (or residuals) between two SCEs is influenced by the values of Umbra-derived SCE, the homoscedasticity between two SCEs is examined with Breusch-Pagan and White tests. Resultantly, both tests yield a p-value considerably smaller than 0.001 and thus reject the null hypothesis that the variance of the residuals is a constant across different independent variable values, i.e., the Umbra-based SCE. Therefore, the presence of heteroscedasticity is confirmed. Notably, it would not alter the values of the previously estimated linear regression model's R-squared value and three correlation coefficients, as they quantify the proportion of explained variance and the overall relationship between two SCEs, regardless of the distribution of residuals. However, the standard errors and the resulting p-values of the parametric Pearson's correlation (nonparametric correlation measures are robust to heteroscedasticity) and regression model's overall F-test might be inflated or deflated, potentially resulting in a misinterpretation of the significance of the relationship and the model's predictive capability.

Finally, step five analyzes the trend and magnitude of the varying correlation between two SCEs after confirming the presence of heteroscedasticity. Firstly, a segmented correlation analysis is performed. It is achieved by dividing the entire data based on the quantiles of the Umbra-derived SCE and calculating the Spearman's correlation of each subset, which results are illustrated in Fig. 4. Clearly, correlation coefficients considerably change with the values of the Umbra-based SCE. By exploring the trends of different numbers of quantiles, it is revealed that the correlation becomes stronger and more significant with increasing Umbra-based SCE values, except for the subset with the smallest quantile. For instance, in the three-quantile scenario, Spearman's correlation coefficients for the middle and high quantile subsets are 0.16 and 0.66, respectively. In the four- (-0.10, 0.31, and 0.61) and five-quantile (-0.01, 0.21, 0.37, and 0.46) scenarios, a similar increasing trend of correlations with the Umbra-based SCE is also observed. Furthermore, statistical significance also increases with the Umbra-based SCE, exemplified by the p-values of the five-quantile scenario that remarkably decrease from larger than 0.05 and 0.01 to smaller than 0.001.

https://doi.org/10.5194/egusphere-2024-1099
Preprint. Discussion started: 16 May 2024

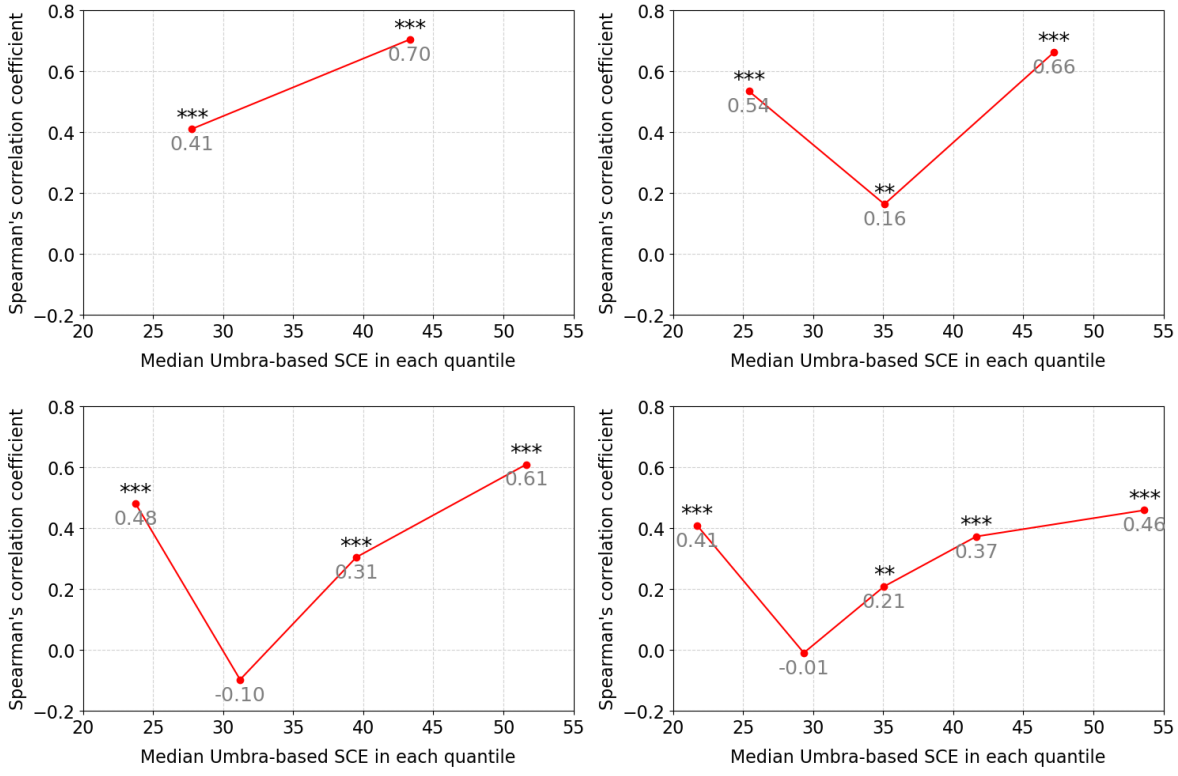

Figure 4: Results of the segmented correlation analysis conducted with different numbers of quantiles of Umbra-based SCE. Correlations with significance at α < 0.05, 0.01, and 0.001 are denoted with *, **, and *.**

Subsequently, conditional quantile regression is conducted by dividing the data according to the quantiles of the Sentinel-1-derived SCE and performing regression for each subset. Founded on the results plotted in Fig. 5, first, it is observed that the slopes of all regression lines (i.e., coefficients of the Umbra-derived SCE) are positive and statistically significant (p-values considerably smaller than 0.001), indicating the consistent and robust positive linear relationship between two SCEs in every quantile subset. Second, since the regression lines of these subsets are not perfectly parallel, the relationship between two SCEs varies with the values, confirming the presence of heteroscedasticity. Particularly, their slopes generally exhibit a gradually increasing trend from the lowest to highest quantiles (0.59, 0.70, 0.86, 0.89, and 0.81 for the 10^{th}, 30^{th}, 50^{th}, 70^{th}, and 90^{th} quantiles, respectively), suggesting that the positive relationship between two SCEs is strengthened at large values. These findings are consistent with the varying magnitudes of positive Spearman's correlation coefficients revealed in the previous segmented correlation analysis.

https://doi.org/10.5194/egusphere-2024-1099
Preprint. Discussion started: 16 May 2024

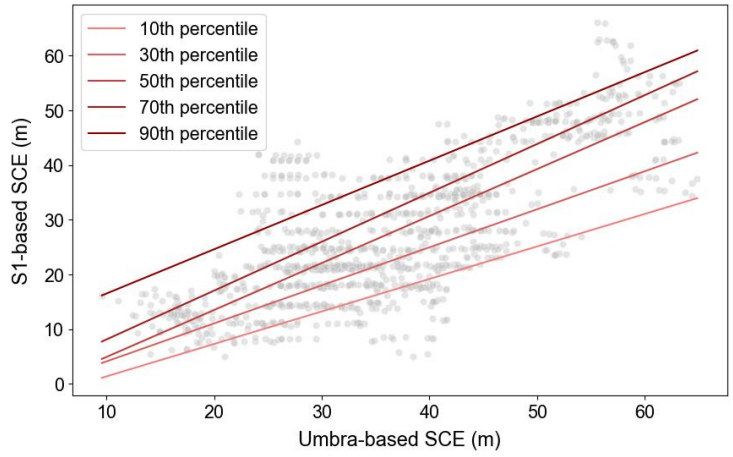

Figure 5: Results of the conditional quantile regression conducted with different numbers of quantiles of Sentinel-1-based SCE. The lines with gradient red colors represent the linear regression line of each quantile subset.

In general, and more importantly, these observations lead to the conclusion that the agreement between two SCEs increases with the magnitude of the SCE. That is, when the SCE becomes larger, the difference between two SCEs is more minor. This study believes it can be explained in two-fold aspects: (1) a significant shoreline movement can be identified by both coarse- and high-resolution SAR images (leading to a small discrepancy between two SCEs), while a trivial movement is challenging to be accurately depicted by Sentinel-1 but only by Umbra images. Therefore, when the actual SCE is small, the Sentinel-1-derived SCE would underestimate the value, causing a greater bias than the more accurate Umbra-derived SCE and resulting in a larger discrepancy between the two SCEs. This assumption can be supported by the underestimation found in the established linear regression model in step two. (2) Shoreline movements more significant than a few pixels can be more easily differentiated from SAR speckle-caused fluctuations on shoreline positions, which are also at a few-pixel scale (Tsai et al., 2023). It can be exemplified by the weak correlations of subsets having Umbra-based SCEs of approximately 30 m (i.e., about 1.5 pixels of the Sentinel-1 images) shown in Fig. 4. Practically, these two conditions can occur simultaneously. Additionally, the microsatellite SAR image co-registration step may also contribute to some uncertainties.

Noticeably, an abruptly high correlation is observed in the smallest quantile subset in the segmented correlation analysis (Fig. 4), which seems to violate the previous conclusion. Actually, this exception is associated with the spatial auto-correlation because, geographically, these transects having small Umbra-based SCE values are predominantly located at the eastmost part of the study coast (Fig. 2(a)), as described in Sect. 4.1. This spatial cluster of transects, i.e., outliers, unsurprisingly has a higher internal consistency. This presumption agrees with the increasing trend of slopes in the conditional quantile regression (Fig. 5), which presents no exceptionally steep slope (i.e., high correlation) in the subset with the smallest Sentinel-1-based SCE values, for these transects are much more widely distributed (Fig. 2(b)), i.e., no distinct spatial auto-correlation exists.

https://doi.org/10.5194/egusphere-2024-1099
Preprint. Discussion started: 16 May 2024

4.3 Contributions and limitations of this study

This study utilizes the latest microsatellite SAR images to depict the rapid summertime erosion over an ice-rich permafrost coast in Alaska. It proposes a robust statistical-based scheme to compare the results with conventional coarse-resolution SAR image-derived observations. This novel dataset and approach provide an unprecedented opportunity to monitor the Arctic coasts' heterogeneous spatio-temporal changes. Notwithstanding, this study acknowledges the following constraints and offers potential solutions.

Firstly, the co-registration accuracy of microsatellite SAR images requires a nuanced tuning, e.g., a high-order polynomial warping function, and thus, demands manual inspections, which hinder automatic processing. In fact, based on the author's investigations, it is found that all microsatellite SAR sensors currently available suffer the same issues, i.e., visible spatial offsets between images. This limitation is primarily due to the poor orbital stability of microsatellites compared to conventional large satellites (Morgan et al., 2020). For instance, in order to reduce transmission power and enhance resolution, microsatellites principally operate on lower orbits than large satellites, which can be exemplified by the fact that all five currently available microsatellite SAR sensors, including ICEYE, Capella Space, Umbra Lab, Synspective StriX-1, iQPS QPS-SAR, all operate on orbits at nominal altitudes ranging between 525 and 580 km, while Sentinel-1 orbit at a 693 km altitude. Therefore, they are more susceptive to atmospheric drag (Urata et al., 2018), directly resulting in a much shorter lifetime. More importantly, the disturbances of the atmosphere would disturb the platform altitude control and antenna pointing capability, especially considering the small size and light weight of microsatellites. Fortunately, many studies aim to overcome this issue by improving designs of altitude and orbit control systems (AOCS) and propulsion systems, which are expected to be soon applied to SAR microsatellites.

Secondly, because the Umbra images used in the present study are geocoded GeoTIFFs, no pre-processing or correction can be performed in the original slant-range geometry. Whilst this product format guarantees the simplicity to handle and visualize SAR data, in the meantime, it inevitably limits the flexibility in processing (e.g., different options for radiometric calibration, terrain-flattening, speckle-filtering, and range-Doppler correction) and thus introduces potential biases. However, so far, most microsatellite SAR companies provide images in this manner (i.e., level 1 amplitude products), e.g., Capella Space provides GEC and geocoded terrain-corrected (GEO) products. In fact, all five currently available microsatellite SAR sensors also offer the information stored in the conventional single look-complex (SLC) products (i.e., amplitude and phase at full native resolution). Nonetheless, they are principally provided in the format of sensor-independent complex data (SICD), that is, a standard developed by the U.S. National Geospatial-Intelligence Agency (NGA) (except ICEYE and Synspective offer alternative options with the common HDF5 and CEOS formats, respectively). Although the SICD format processed using the polar format algorithm (PFA) is commonly used by defense applications, it is rarely adopted by the earth observation remote sensing community, which prefers the standard 0-Doppler slant-range-azimuth geometry to annotate the focused data. Consequently, conventional SAR-processing software does not support the SICD images. Fortunately, due to the rapid blooming and growing needs of microsatellite SAR data, recently many commercial software (such as GAMMA v20211201,

https://doi.org/10.5194/egusphere-2024-1099
Preprint. Discussion started: 16 May 2024

Socet GXP v4.4, and ENVI SARscape v5.6) have developed the corresponding data readers to digest SICD format (although not all guarantee the further processing capability). Unfortunately, most open-source software, including the popular Sentinel Application Platform (SNAP), does not support this format yet (except the SarPy Python library released by NGA).

Lastly, apart from exploiting the ultra-fine spatial resolution of microsatellite SAR data, the benefits of their high temporal resolution for Arctic coast monitoring should also be investigated. Since this study aims to depict the shoreline retreating during the summer, Umbra images are acquired bi-weekly. Nevertheless, more frequent temporal sampling is required if researchers or stakeholders aim to observe short-term spatio-temporal dynamics. Thankfully, as Umbra Lab currently has eight satellites in operation, a daily revisit is guaranteed. Moreover, considering the high latitude of Arctic coasts and the nature of near-polar orbits, the revisit time is further reduced. In fact, this much shorter repeat cycle compared to the modern large SAR satellites' bi-week revisit is available for all five microsatellite SAR constellations mentioned before, as they operate on a much lower orbit height. Practically, a sub-daily image acquisition greatly facilitates tracking block failure events (i.e., segments of bluffs detaching from the coast and collapsing) caused by thermo-abrasion, which is the predominant failure mechanism in the ice-rich Alaskan coasts (Ravens et al., 2012), because the entire block toppling and disintegrating processes often take less than a week. To monitor this short-term change, conventional studies usually rely on field observations, such as Unmanned aerial vehicle (UAV)-based imagery (Thomas et al., 2020) or time-lapse camera-based imagery (Barnhart et al., 2014; Jones et al., 2009). Thankfully, employing the microsatellite images and the approach demonstrated in this study guarantees a feasible alternative for high-frequency Arctic coast monitoring.

5 Conclusions

The present study employs the latest microsatellite SAR data to depict the summertime coastal erosion on an ice-rich Arctic coast. On the basis of the proposed multi-stage statistical-driven workflow, microsatellite SAR-derived results are robustly compared with the observations derived from the conventional coarse-resolution SAR data. A statistically significant positive relationship between the two results with the presence of heteroscedasticity is confirmed. Specifically, the agreement between the two results increases with the magnitude of retreating distance, suggesting that the microsatellite SAR can depict more detailed changes in the coastal landscape. Although currently, microsatellite SAR exhibits technical immatureness, such as poor orbital stability and software-handled capacity, grounded on the unprecedented results and analysis achieved in this study, their valuable benefits and promising uniqueness for depicting coastal spatio-temporal dynamics are clearly highlighted.

Data availability

Some data that support the findings of this study are available from the corresponding author upon reasonable request.

Author contribution

Y.T. designed the experiments and prepared the manuscript.

Competing interests

The author declares that there is no conflict of interest.

https://doi.org/10.5194/egusphere-2024-1099
Preprint. Discussion started: 16 May 2024

Acknowledgements

This study was funded by the National Science and Technology Council (NSTC) under grant number 112-2121-M-002-001 and the Yushan Fellow Program by the Ministry of Education (MOE) under grant number NTU-112V1022-2. TerraSAR-X data used in this study were kindly provided by DLR under the Science proposal ID: COA3893.

References

Angelliaume, S., Dubois-Fernandez, P. C., Jones, C. E., Holt, B., Minchew, B., Amri, E., and Miegebielle, V.: SAR imagery for detecting sea surface slicks: Performance assessment of polarization-dependent parameters, IEEE Transactions on Geoscience and Remote Sensing, 56, 4237-4257, 2018.

Anghel, A., Cacoveanu, R., Moldovan, A.-S., Rommen, B., and Datcu, M.: COBIS: Opportunistic C-band bistatic SAR differential interferometry, IEEE Journal of Selected Topics in Applied Earth Observations and Remote Sensing, 12, 3980-3998, 2019.

Barnhart, K. R., Anderson, R. S., Overeem, I., Wobus, C., Clow, G. D., and Urban, F. E.: Modeling erosion of ice-rich permafrost bluffs along the Alaskan Beaufort Sea coast, Journal of Geophysical Research: Earth Surface, 119, 1155-1179, 2014.

Bartsch, A., Ley, S., Nitze, I., Pointner, G., and Vieira, G.: Feasibility study for the application of Synthetic Aperture Radar for coastal erosion rate quantification across the Arctic, Frontiers in Environmental Science, 8, 143, 2020.

Bishara, A. J. and Hittner, J. B.: Confidence intervals for correlations when data are not normal, Behavior research methods, 49, 294-309, 2017.

Bishara, A. J. and Hittner, J. B.: Testing the significance of a correlation with nonnormal data: comparison of Pearson, Spearman, transformation, and resampling approaches, Psychological methods, 17, 399, 2012.

Bodansky, E., Gribov, A., and Pilouk, M.: Smoothing and compression of lines obtained by raster-to-vector conversion, 2002, 256-265.

Bristol, E. M., Connolly, C. T., Lorenson, T. D., Richmond, B. M., Ilgen, A. G., Choens, R. C., Bull, D. L., Kanevskiy, M., Iwahana, G., and Jones, B. M.: Geochemistry of coastal permafrost and erosion-driven organic matter fluxes to the Beaufort Sea near Drew Point, Alaska, Frontiers in Earth Science, 8, 598933, 2021.

Ferrer-Valero, N.: Measuring geomorphological diversity on coastal environments: A new approach to geodiversity, Geomorphology, 318, 217-229, 2018.

Frederick, J. M., Thomas, M. A., Bull, D. L., Jones, C. A., and Roberts, J. D.: The Arctic coastal erosion problem, Sandia National Lab.(SNL-NM), Albuquerque, NM (United States), 2016.

Frohn, R. C., Hinkel, K. M., and Eisner, W. R.: Satellite remote sensing classification of thaw lakes and drained thaw lake basins on the North Slope of Alaska, Remote sensing of environment, 97, 116-126, 2005.

https://doi.org/10.5194/egusphere-2024-1099
Preprint. Discussion started: 16 May 2024

Geudtner, D., Prats, P., Yague-Martinez, N., Navas-Traver, I., Barat, I., and Torres, R.: Sentinel-1 SAR interferometry performance verification, 2016, 1-4.

Gibbs, A. E. and Richmond, B. M.: National assessment of shoreline change: historical shoreline change along the north coast of Alaska, US-Canadian border to Icy Cape, US Department of the Interior, US Geological Survey Washington, DC, USA, 2015.

Guo, D. and Wang, H.: CMIP5 permafrost degradation projection: A comparison among different regions, Journal of Geophysical Research: Atmospheres, 121, 4499-4517, 2016.

Himmelstoss, E., Farris, A., Henderson, R., Kratzmann, M., Ergul, A., Zhang, O., Zichichi, J., and Thieler, E.: Digital Shoreline Analysis System (version 5.0): US Geological Survey software. 2018.

Jones, B. M., Arp, C. D., Beck, R. A., Grosse, G., Webster, J. M., and Urban, F. E.: Erosional history of Cape Halkett and contemporary monitoring of bluff retreat, Beaufort Sea coast, Alaska, Polar Geography, 32, 129-142, 2009.

Jones, B. M., Farquharson, L. M., Baughman, C. A., Buzard, R. M., Arp, C. D., Grosse, G., Bull, D. L., Günther, F., Nitze, I., and Urban, F.: A decade of remotely sensed observations highlight complex processes linked to coastal permafrost bluff erosion in the Arctic, Environmental Research Letters, 13, 115001, 2018.

Jorgenson, M. and Brown, J.: Classification of the Alaskan Beaufort Sea Coast and estimation of carbon and sediment inputs from coastal erosion, Geo-Mar. Lett., 25, 69-80, 2005.

Marquez-Neila, P., Baumela, L., and Alvarez, L.: A morphological approach to curvature-based evolution of curves and surfaces, IEEE Transactions on Pattern Analysis and Machine Intelligence, 36, 2-17, 2013.

Morgan, J., Boudreau, A., Verdugo, M., Meloni, F., and Colombo, D.: New satellite sensors for monitoring mining areas: a look at the future, 2020, 1521-1530.

Nicolsky, D. J., Romanovsky, V. E., Panda, S. K., Marchenko, S. S., and Muskett, R. R.: Applicability of the ecosystem type approach to model permafrost dynamics across the Alaska North Slope, Journal of Geophysical Research: Earth Surface, 122, 50-75, 2017.

Patyuchenko, A., Younis, M., Sigurd, H., Bordoni, F., and Krieger, G.: Design aspects and performance estimation of the reflector based digital beam-forming SAR system, 2009.

Philipp, M., Dietz, A., Ullmann, T., and Kuenzer, C.: Automated extraction of annual erosion rates for Arctic permafrost coasts using Sentinel-1, deep learning, and change vector analysis, Remote Sensing, 14, 3656, 2022.

Ravens, T. M., Jones, B. M., Zhang, J., Arp, C. D., and Schmutz, J. A.: Process-based coastal erosion modeling for drew point, North Slope, Alaska, Journal of Waterway, Port, Coastal, and Ocean Engineering, 138, 122-130, 2012.

Sayre, R., Noble, S., Hamann, S., Smith, R., Wright, D., Breyer, S., Butler, K., Van Graafeiland, K., Frye, C., and Karagulle, D.: A new 30 meter resolution global shoreline vector and associated global islands database for the development of standardized ecological coastal units, Journal of Operational Oceanography, 12, S47-S56, 2019.

https://doi.org/10.5194/egusphere-2024-1099
Preprint. Discussion started: 16 May 2024

Stocker, T. F., Qin, D., Plattner, G., Tignor, M., Allen, S., Boschung, J., Nauels, A., Xia, Y., Bex, V., and Midgley, P.: Contribution of working group I to the fifth assessment report of the intergovernmental panel on climate change, Climate change, 2013. 2013.

Streletskiy, D., Anisimov, O., and Vasiliev, A.: Permafrost degradation. In: Snow and ice-related hazards, risks and disasters, Elsevier, 2015.

Thomas, M. A., Mota, A., Jones, B. M., Choens, R. C., Frederick, J. M., and Bull, D. L.: Geometric and material variability influences stress states relevant to coastal permafrost bluff failure, Frontiers in Earth Science, 8, 143, 2020.

Tsai, Y.-L. S.: Monitoring Arctic Permafrost Coastal Erosion Dynamics Using a Multidecadal Cross-mission SAR Dataset Along an Alaskan Beaufort Sea Coastline, Sci. Tot. Environ., 917, 170389, 2024.

Tsai, Y.-L. S., Huang, C.-J., Chen, C.-L., and Han, J.-Y.: Automatic Monitoring of Oil Tank 3D Geometry and Storage Changes with Interferometric Coherence and SAR Intensity Information, IEEE Journal of Selected Topics in Applied Earth Observations and Remote Sensing, 2023. 2023.

Tsai, Y.-L. S. and Tseng, K.-H.: Monitoring multidecadal coastline change and reconstructing tidal flat topography, International Journal of Applied Earth Observation and Geoinformation, 118, 103260, 2023.

Urata, K. N., Sri Sumantyo, J. T., Santosa, C. E., and Viscor, T.: Development of an L-band SAR microsatellite antenna for earth observation, Aerospace, 5, 128, 2018.

Wegner, C., Bennett, K. E., de Vernal, A., Forwick, M., Fritz, M., Heikkilä, M., Łącka, M., Lantuit, H., Laska, M., and Moskalik, M.: Variability in transport of terrigenous material on the shelves and the deep Arctic Ocean during the Holocene, Polar Res., 34, 24964, 2015.

Xu, Z., Shi, Q., Chen, Y., Feng, W., Shao, Y., Sun, L., and Huang, X.: Non-stationary speckle reduction in high resolution SAR images, Digital Signal Processing, 73, 72-82, 2018.